IFASD 2015
International Forum on Aeroelasticity and Structural Dynamics
June 28 — July 02, 2015 ▲ Saint Petersburg, Russia

Aircraft Dynamic Loads with Varying Geometry and Flight Mechanics Effects

Moti Karpel[1] and **Aviv Romm**[2]
Faculty of Aerospace Engineering, Technion, Haifa 32000, Israel
and
Manuel Reyes[3] and **Hector Climent**[4]
Airbus Defence & Space, 28906 Getafe (Madrid) Spain

Keywords: Structural dynamics. Increased-order modeling. Morphing.

Abstract: The increased-order modeling (IOM) approach and the related Dynresp aeroservoelastic simulation framework are expanded to include general frequency-domain sensors and generalized force feedback. The expansion facilitates efficient applications to nonlinear gust-response simulations of flight vehicles while changing their wing sweep angle, the structural coupling between components and with flight mechanic effects that are normally not taken into account in common dynamic loads analyses. The new general sensors are employed to express current generalized unsteady aerodynamic forces as response parameters during the simulations. The responses are combined for time-domain response surfaces using Inverse Fast Fourier Transforms. Interpolations in the response surfaces according to the prescribed sweep-angle variation allow gust response simulations while the wing sweep angle is changing, causing continuous changes in the aerodynamic panel model. A modal coupling technique that is based on interface fictitious masses is used for defining the interface forces that satisfy the displacement compatibility constraints while accounting for the relative rotations between structural components. The forces are applied in terms of time-domain changes in the generalized mass matrix. The feedback force capabilities are used also for introducing flight-mechanic forces, such as induced drag, gravity effects and changes in local velocities due to yaw. The new capabilities are demonstrated in two test cases: (a) dynamic response of an aircraft to discrete gust during changes in the wing sweep angle; and (b) dynamic response of a transport aircraft to continuous turbulence and maneuver commands with rigid-body flight mechanic effects.

1 INTRODUCTION

The calculation of aircraft loads in response to gusts and turbulence is usually separated into steady and dynamic contributions. These two are generally uncoupled and allow for the standard approach where different models and methodologies are used for each one. This paper deals with dynamic loads that are calculated in the industry using modal methods relying on linear structural and aerodynamic models (referred hereafter as the aeroelastic model). The common methodology is expanded to deal with significant non-standard varying geometry and flight-mechanic effects and with excitation cases where the energy of the excitation lies on the validity boundaries of the model such as in continuous turbulence.

[1] Professor, Sanford Kaplan Chair for Aerospace Engineering. AIAA Fellow.
[2] Graduate student.
[3] Dynamic specialist
[4] Head of Structural Dynamics and Aeroelasticity Domain

Generally speaking the linear hypothesis implies that the model geometry does not change in time and that forces do not follow the deformation. This means, for instance, that lift is always perpendicular to the initial position of the lifting surface. Continuing with the unsteady aerodynamic forces, they are calculated using a Doublet-Lattice method model, consisting of an adequate number of aerodynamic boxes. Each box generates lift perpendicular to its plane and a pitch moment. Forces and moments in directions other than local heave and pitch are not taken into account. These methodology limitations are of no importance in most problems, in particular in gust response where the mentioned models are considered proven, robust and rapid. They are designed to correctly represent the aircraft dynamic behavior up to a frequency of about 50 Hz, for a typical transport aircraft.

The increased-order modeling (IOM) approach[1,2], utilized in the Dynresp aeroservoelastic simulation code, supplement common linear frequency-domain (FD) models with time-domain (TD) feedback loops that simulate nonlinear effects or configuration changes. The Dynresp code has been employed for various industrial loads applications with nonlinear elements. Among the industrial applications were dynamic loads with nonlinear control system[3] and gust response of transport aircraft with free play in the elevator actuators[4]. The procedure is expanded in this paper to accommodate model changes during the simulation that are associated with the aerodynamic geometry, with the coupling between structural components and with linear flight-mechanic effects that are normally not taken into account.

Dynamic response simulations can be based on state-space time-domain equations, modified to agree with flight-mechanic coefficients obtained from other sources such as wind-tunnel measurements or CFD[5]. Being based on rational approximations of the unsteady aerodynamic force coefficient matrices, such models are usually not compatible with common industrial dynamic loads procedures. Other response simulations of morphing vehicles, such as the rotating wing in Ref. 6, were based on CFD. The structural dynamic part of Ref. 6 used modal coupling of the separately calculated body and wing modes obtained with fictitious masses added at the wing-body interface degrees of freedom[7,8]. A similar modal-coupling approach is used in this paper to obtain high-accuracy interface compatibility. However, instead of a continuous modification of the generalized mass matrix, the nonlinear feedback loop of Dynresp is used for introducing the equivalent inertial forces based on sensed modal accelerations. A static version of this modal coupling procedure was applied in Ref. 9.

The aerodynamic changes are introduced by generating simultaneous response surfaces at various flight conditions. Interpolation between the response curves and the application of feedback forces modify the aerodynamic forces during the simulation. As detailed in the following sections, the aerodynamic response parameters are based on FD numerical sensors whose outputs transformed to TD using IFFT, which facilitates continuous application of aerodynamic force changes in the TD feedback according to current sweep angles.

The new capabilities are demonstrated in two test cases: (a) dynamic response of a morphing aircraft to discrete gust during changes in the wing sweep angle; and (b) dynamic response of a transport aircraft to continuous turbulence and maneuver commands with rigid-body flight mechanic effects. Dynamic loads associated with the aeroelastic response are calculated using the mode-displacement approach[10] that is based on the time varying modal displacements. The application of fictitious masses was shown in Ref. 11 to yield very accurate mode-displacement section loads.

2 THE IOM PROCESS

The IOM framework used in this work presents systematic methodology and computational tools that exploit the numerical advantages in dealing with linear systems while keeping the complexity of the added nonlinear elements as low as required for obtaining adequate accuracy in aeroelastic analysis. The model, schematically depicted in Figure 1, is based on a main linear block that is stable when disconnected from the nonlinear elements, and a nonlinear block that expresses all the nonlinearities as feedback loops. The response calculations are performed in 3 stages: (a) response of the linear block with the nonlinear block disconnected; (b) addition of nonlinear effects using nonlinear elements and convolution integrals; and (c) complementary response of the linear block to inputs from the nonlinear block to generate the final output.

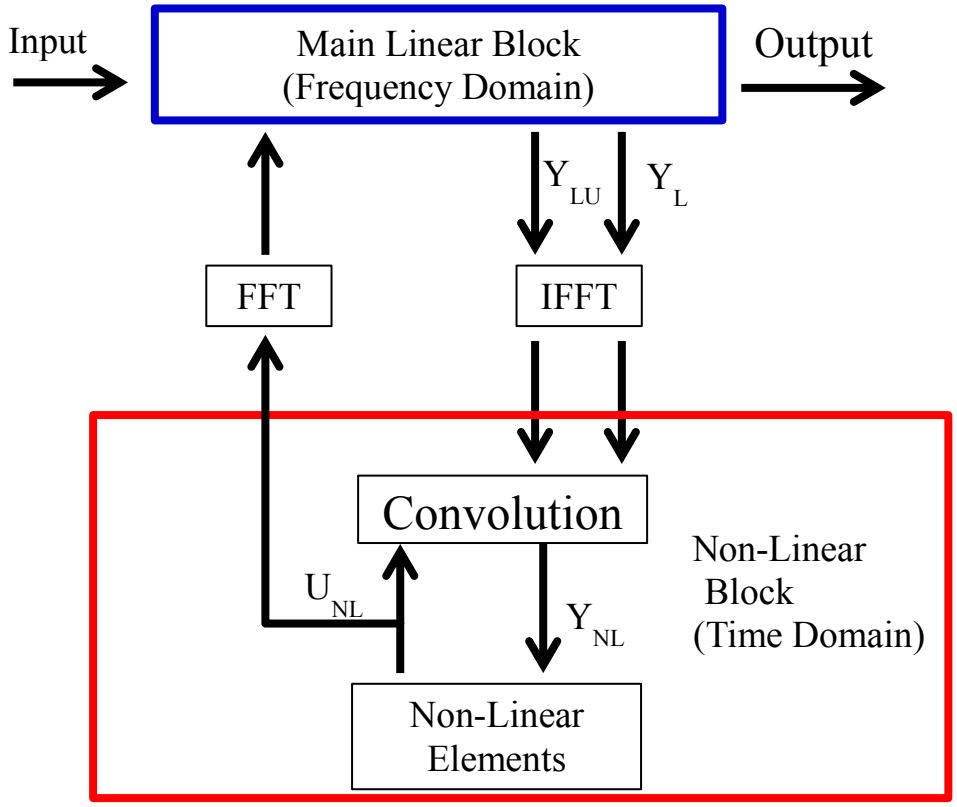

Figure 1: Block Diagram of the simulation process in Dynresp

The nonlinear block is used in our case for changing the modal coupling terms and the generalized aerodynamic forces when the sweep angle changes, as detailed in the following sections. The input is a symmetric uniform "1-cos" vertical-gust front.

The first stage is performed in the linear block in Figure 1, based on frequency-domain (FD) response to external excitation. With no control system, the modal response is obtained by solving

$$\left[A(i\omega)\right]\left\{\xi_L(i\omega)\right\} = \left\{B(i\omega)\right\}\frac{w_G(i\omega)}{V} \tag{1}$$

where $\left[A(i\omega)\right] = -\omega^2\left[M_{hh}\right] + i\omega\left[B_{hh}\right] + \left[K_{hh}\right] + q\left[Q_{hh}(i\omega)\right]$; $\left\{B(i\omega)\right\} = -q\left\{Q_{hG}(i\omega)\right\}$

where $\{\xi_L(i\omega)\}$ is the FD modal displacements, $w_G(i\omega)$ is obtained by FFT of the input gust velocity profile $w_G(t)$ and V is the flight velocity. $[A(i\omega)]$ includes the generalized mass, damping, stiffness and aerodynamic matrices and *q* is the dynamic pressure. $\{Q_{hG}(i\omega)\}$ is the vector of FD generalized forces due to unit-amplitude angles of attack induced by the gust velocity. To allow the use of IFFT to transform the results into TD, the system has to be dynamically stable at the analyzed flight conditions. The ω=0 case, where $[A(0)]$ is normally singular in rigid-body motion, presents a special problem that is resolved in Dynresp by either enforcing zero initial displacements or loads without calculating $\{\xi_L(0)\}$, or transforming the rigid-body displacements to flight-mechanic states[12].

The outputs $y_L(i\omega)$ of the main linear block in Fig. 1, which are inputs to the nonlinear block, can be generally expressed as

$$\{y_L(i\omega)\} = [C(i\omega)]\{\xi_L(i\omega)\} + \{D(i\omega)\}\frac{w_G(i\omega)}{V} \tag{2}$$

Frequency response of the displacement vectors $\{\xi_L(i\omega)\}$ to unit inputs $u_{NL}(i\omega)$ from the nonlinear block are arranged in the $[x_{LU}(i\omega)]$ matrix and calculated by

$$[x_{LU}(i\omega)] = [A(i\omega)]^{-1}[B_{NL}(i\omega)] \tag{3}$$

from which selected frequency-response functions $y_{LU}(i\omega)$ of the linear output vector to unit inputs from the nonlinear block are calculated by

$$[y_{LU}(i\omega)] = [C_{LU}(i\omega)][x_{LU}(i\omega)] + [D_{LU}(i\omega)] \tag{4}$$

To complete the first stage and generate the interim outputs of the linear block in Figure 1, the linear FD responses of Eqs. (2) and (4) are transformed to TD by

$$\{y_L(t)\} = IFFT\{y_L(i\omega)\} \tag{5}$$

and

$$[y_{LU}(t)] = IFFT[y_{LU}(i\omega)] \tag{6}$$

The second stage is performed in the nonlinear block of Figure 1. The time *t* is set back to zero and a time-marching nonlinear computation of the outputs $u_{NL}(t)$ of the nonlinear block is performed in consecutives time steps. The outputs $\{y_L(t)\}$ of the linear block are amended in each time step by the convolution integral

$$\{y_{NL}(t)\} = \{y_L(t)\} + \int_0^t [y_{LU}(t-\tau)]\{u_{NL}(\tau)\}\,d\tau \tag{7}$$

and serve as inputs to the nonlinear functions (NLF) in the following time step

$$\{u_{NL}(t)\} = NLF\{y_{NL}(t)\} \tag{8}$$

The computation process returns in the third stage to the linear block of Figure 1. The second-stage output $\{u_{NL}(t)\}$ of Eq. (8) is converted to FD by FFT and the final response is calculated by

$$\{\xi_{NL}(i\omega)\} = \{\xi_L(i\omega)\} + [A(i\omega)]^{-1}[B_{NL}(i\omega)]\{u_{NL}(i\omega)\} \tag{9}$$

followed by

$$\{\xi_{NL}(t)\} = IFFT\{\xi_{NL}(i\omega)\} \tag{10}$$

This final TD state response may be used for calculating any desired output that is a function of $\{x_{NL}(t)\}$ within Dynresp, or exported for subsequent loads calculations.

3 MODAL COUPLING WITH FICTITIOUS MASSES

The simulation of gust response while the vehicle wings change their sweep angle is performed in this paper with the generalized coordinates in Eq. (1) based on separate sets of normal modes for the right wing and for the body-tail substructures. Only symmetric modes of the body-tail unit are taken into account such that the resulting coupled motion is symmetric. The separate modes are calculated with fictitious masses loading the wing-body statically determined interface coordinates in each substructure. The modal coupling process formulated in this section sets the equations of motion, removes the fictitious-mass effects and apply displacement compatibility equations at the interface points to yield the coupled equations of motion.

The body-tail finite-element mass and stiffness matrices, $\bar{M}_B$ and $\bar{K}_B$, partitioned into body (B) and interface (I) coordinates, are used for setting the eigenvalues problems for extracting the separate body-tail modes

$$\begin{bmatrix} \bar{M}_{BB} & \bar{M}_{BI} \\ \bar{M}_{BI}^T & \bar{M}_{II}^{(B)} + \bar{M}_F^{(B)} \end{bmatrix} \begin{bmatrix} \Phi_B \\ \Phi_{BI} \end{bmatrix} \left[\Omega_B^2\right] = \begin{bmatrix} \bar{K}_{BB} & \bar{K}_{BI} \\ \bar{K}_{BI}^T & \bar{K}_{II}^{(B)} \end{bmatrix} \begin{bmatrix} \Phi_B \\ \Phi_{BI} \end{bmatrix} \tag{11}$$

which are solved for the uncoupled low-frequency body normal modes $[\Phi_B]$ and the diagonal natural frequency $[\Omega_B]$ matrix. $\bar{M}_F^{(B)}$ contains the fictitious masses added to the 6 interface coordinates. The first 3 frequencies in $[\Omega_B]$ are zero for the 3 symmetric rigid-body modes. Similar equations are solved for the separate wing modes and frequencies $[\Phi_W]$ and $[\Omega_W]$ that include 6 rigid-body modes. In the formulation below, these body and wing modes are normalized to unit generalized mass.

The modal equations of motion of the two substructures are first combined for a unified uncoupled free un-damped equation, with the fictitious masses removed,

$$\begin{bmatrix} M_B & 0 \\ 0 & M_W \end{bmatrix} \begin{Bmatrix} \ddot{\xi}_B \\ \ddot{\xi}_W \end{Bmatrix} + \begin{bmatrix} \Omega_B{}^2 & 0 \\ 0 & \Omega_W{}^2 \end{bmatrix} \begin{Bmatrix} \xi_B \\ \xi_W \end{Bmatrix} = \{0\} \tag{12}$$

where the stiffness matrix is diagonal but the mass matrix is not,

$$[M_B] = [I] - [\Phi_{BI}]^T \left[\bar{M}_F^{(B)}\right][\Phi_{BI}]; \quad [M_W] = [I] - [\Phi_{WI}]^T \left[\bar{M}_F^{(W)}\right][\Phi_{WI}]$$

The modal coordinates of Eq. (12) are related to the discrete coordinates by

$$\begin{Bmatrix} u_B \\ u_{IB} \\ u_W \\ u_{IW} \end{Bmatrix} = \begin{bmatrix} \Phi_B & 0 \\ \Phi_{BI} & 0 \\ 0 & \Phi_W \\ 0 & \Phi_{WI} \end{bmatrix} \begin{Bmatrix} \xi_B \\ \xi_W \end{Bmatrix} \tag{13}$$

where the wing displacements are defined at the wing local coordinate system. Compatibility between the interface displacements $\{u_{IB}\}$ and $\{u_{IW}\}$ implies the constraint equation

$$[\Phi_{WI}]\{\xi_W\} = [T_R][\Phi_{BI}]\{\xi_B\} \tag{14}$$

where $\{\xi_W\}$ includes rigid and elastic modes, $\{\xi_W^{(r)}\}$ and $\{\xi_W^{(e)}\}$, and rotation transformation is

$$[T_R] = \begin{bmatrix} \cos(\Lambda) & \sin(\Lambda) & 0 & 0 & 0 & 0 \\ -\sin(\Lambda) & \cos(\Lambda) & 0 & 0 & 0 & 0 \\ 0 & 0 & 1 & \cos(\Lambda) & \sin(\Lambda) & 0 \\ 0 & 0 & 0 & -\sin(\Lambda) & \cos(\Lambda) & 0 \\ 0 & 0 & 0 & 0 & 0 & 1 \end{bmatrix} \tag{15}$$

where Λ is the sweep angle, which is also, in our case, the rotation angle between the wing and body coordinate systems. Eq. (14) implies the transformation from the uncoupled modal displacements to the coupled ones

$$\{\xi\} = [T]\{\xi_h\} \tag{16}$$

where

$$\{\xi\} = \begin{Bmatrix} \xi_B \\ \xi_W^{(r)} \\ \xi_W^{(e)} \end{Bmatrix}; \qquad [T] = \begin{bmatrix} I & 0 \\ \Phi_{WI}^{(r)^{-1}} T_R \Phi_{BI} & -\Phi_{WI}^{(r)^{-1}} \Phi_{WI}^{(e)} \\ 0 & I \end{bmatrix}; \qquad \{\xi_h\} = \begin{Bmatrix} \xi_B \\ \xi_W^{(e)} \end{Bmatrix} \tag{17}$$

The number of modal degrees of freedom is reduced as the wing rigid modes $\xi_W^{(r)}$ become dependent. By the substitution of Eq. (16) in Eq. (12) and pre-multiplication by $[T]^T$, a full coupled model structural equation of motion is obtained,

$$[M_{hh}(\Lambda)]\{\ddot{\xi}_h\} + [K_{hh}]\{\xi_h\} = \{0\} \tag{18}$$

where

$$[M_{hh}(\Lambda)] = [T(\Lambda)]^T \begin{bmatrix} M_B & 0 \\ 0 & M_W \end{bmatrix} [T(\Lambda)]; \quad [K_{hh}] = \begin{bmatrix} \Omega_B{}^2 & 0 \\ 0 & \Omega_W^{(e)2} \end{bmatrix}$$

where $\Omega_W^{(e)}$ is Ω_W of Eq. (12), but with the 6 all-zero rows and columns related to the rigid modes removed. The modal displacements of Eq. (18) are related to the discrete displacements of the coupled structure by

$$\begin{Bmatrix} u_B \\ u_{IB} \\ u_W \end{Bmatrix} = [\Phi_h] \begin{Bmatrix} \xi_B \\ \xi_W^{(e)} \end{Bmatrix} \tag{19}$$

where

$$[\Phi_h] = \begin{bmatrix} \Phi_B & 0 & 0 \\ \Phi_{BI} & 0 & 0 \\ 0 & \Phi_W^{(r)} & \Phi_W^{(e)} \end{bmatrix} [T] = \begin{bmatrix} \Phi_B & 0 \\ \Phi_{BI} & 0 \\ \Phi_W^{(r)}\Phi_{WI}^{(r)-1}T_R\Phi_{BI} & \Phi_W^{(e)} - \Phi_W^{(r)}\Phi_{WI}^{(r)-1}\Phi_{WI}^{(e)} \end{bmatrix} \tag{20}$$

Equation (18) is expanded in the following section to include damping, aerodynamic and excitation terms. It can also be used for evaluating the coupling process, for which we can perform an eigenvalue analysis with the non-diagonal $[M_{hh}]$ and the diagonal $[K_{hh}]$ of Eq. (18). It yields the natural frequencies $[\tilde{\Omega}]$ and the square matrix of eigenvectors $[\tilde{\psi}]$. $[\tilde{\Omega}]$ and $[\tilde{\Phi}] = [\Phi_h][\tilde{\psi}]$ can be compared to the natural frequencies and mode shapes extracted for the combined structure directly from the finite-element model.

Eq. (18) can be written as

$$[M_{hh}(0)]\{\ddot{\xi}_h\} + [K_{hh}]\{\xi_h\} = -[\Delta M_{hh}(\Lambda)]\{\ddot{\xi}_h\} \tag{21}$$

where $[\Delta M_{hh}(\Lambda)] = [M_{hh}(\Lambda)] - [M_{hh}(0)]$ such that the left side forms the baseline model of the linear block in Figure 1 and the inertial forces at the right side can be defined as feedback forces generated by the nonlinear block.

4 GUST RESPONSE DURING SWEEP ANGLE CHANGE

4.1: Linear response at $\Lambda = 0$

The simulation of aeroelastic response to gust excitation, while the wing sweep angle changes, is divided in the IOM process to a linear response at $\Lambda = 0$ and the incremental response due to scheduled changes in Λ. The FD equation of motion for the linear part is Eq. (1) with $M_{hh}(0)$ and K_{hh} of Eq. (18), and with B_{hh} that reflects a uniform modal coefficient damping of $\zeta = 0.01$. The aerodynamic coefficient matrix $Q_{hh}(i\omega)$ and gust column $Q_{hG}(i\omega)$ in Eq. (1) are generated by an unsteady panel model (ZAERO in our case) at selected frequency values, and interpolated to all the frequency values required for the solution process. The aerodynamic model in ZAERO is first generated for use in Eq. (1) with the aircraft geometry at $\Lambda = 0$, with the respective modes $\Phi_h(0)$ of Eq. (20).

The aerodynamic matrices at other sweep angles are also generated in preparation for the linear run at several sweep angles between 0 and 60 *deg*. The ZAERO aerodynamic panel model at $\Lambda = 30\,deg$ is shown in Figure 2. $Q_{hhi}(i\omega)$ and $Q_{hGi}(i\omega)$ are generated for the selected sweep angles considering the affected aerodynamic model and structural modes $\Phi_h(\Lambda_i)$. They are used in Dynresp for defining the linear outputs of Eq. (2) as

$$\begin{Bmatrix} y_{h1_L}(i\omega) \\ y_{h2_L}(i\omega) \\ \vdots \\ y_{hn_L}(i\omega) \\ y_{acc_L}(i\omega) \end{Bmatrix} = \begin{bmatrix} Q_{hh1}(i\omega) \\ Q_{hh2}(i\omega) \\ \vdots \\ Q_{hhn}(i\omega) \\ -\omega^2 I \end{bmatrix} \left\{ \xi_L(i\omega) \right\} + \begin{Bmatrix} Q_{hG1}(i\omega) \\ Q_{hG2}(i\omega) \\ \vdots \\ Q_{hGn}(i\omega) \\ 0 \end{Bmatrix} \frac{w_G(i\omega)}{V} \tag{22}$$

such that $\left\{ y_{hi_L}(i\omega) \right\}$ reflects the generalized unsteady aerodynamic forces if Λ would change to Λ_i and $\left\{ y_{acc_L}(i\omega) \right\}$ is the vector of generalized accelerations. Similarly to the aerodynamic matrices in Eq. (1), the FD coefficient matrices in Eq. (22) are defined at the selected frequency values and interpolated during the FD solution to all the frequency values at which Eq. (1) is solved.

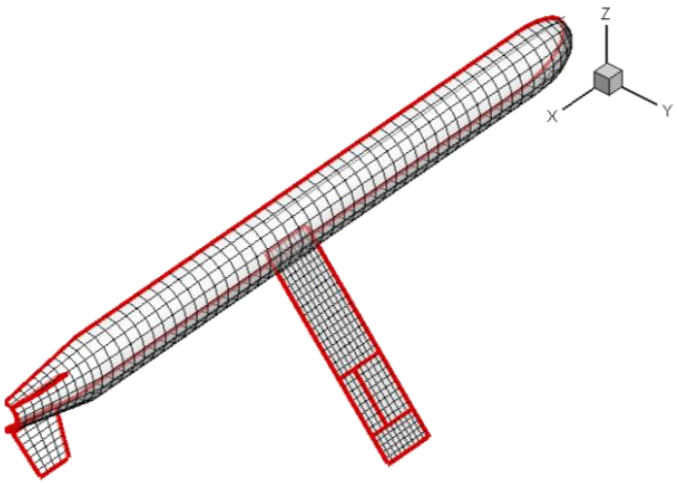

Figure 2: Aerodynamic model at $\Lambda = 30\,deg$

Once the solution $\{\xi_L(i\omega)\}$ and the output $\{y_L(i\omega)\}$ are calculated, they are transformed to TD, $\{\xi_L(t)\}$ and $\{y_L(t)\}$, using IFFT. In addition, the frequency response matrix $[y_{LU}(i\omega)]$ is calculated using Eqs. (3) and (4) with the inputs being unit-amplitude generalized forces and the outputs are those of Eq. (22). IFFT of $[y_{LU}(i\omega)]$ yields the respective impulse response matrix $[y_{LU}(t)]$ for the convolution process in the next section.

4.2: Wing deployment effects

The nonlinear block in Figure 1 is used for adding the effects of changing the sweep angle to the linear solution. Eq. (1) is complemented with the generalized forces associated with the morphing process, which yields

$$[A(i\omega)]\{\xi_{NL}(i\omega)\} = \{B(i\omega)\}\frac{w_G(i\omega)}{V} + \{F_h(i\omega)\} \tag{23}$$

where $F_h(i\omega)$ is the FD counterpart of the generalized force vector

$$\{F_h(t)\} = -[\Delta M_{hh}(\Lambda)]\{y_{acc_{NL}}(t)\} - q\{\Delta y_{h_{NL}}(t)\} \tag{24}$$

where Λ is a prescribed function of *t*. The variables in the right side of Eq. (24) are based on the convolution integral

$$\{y_{NL}(t)\} = \{y_L(t)\} + \int_0^t [y_{LU}(t-\tau)]\{F_h(\tau)\}\, d\tau \tag{25}$$

where $\{y_L(t)\}$ is detailed in Eq. (22), which indicates that the modal acceleration $\{y_{acc_{NL}}(t)\}$ of Eq. (24) is the bottom partition of $\{y_{NL}(t)\}$. The generalized aerodynamic feedback $\{\Delta y_{h_{NL}}(t)\}$ of Eq. (24) is interpolated from the aerodynamic outputs of $\{y_{NL}(t)\}$ in Eq. (25).

The convolution process produces $\{F_h(t)\}$ of Eq. (24), which is transformed at the end to FD using FFT. Eq. (23) can be solved now for the final modal response by using Eq. (9) that becomes

$$\{\xi_{NL}(i\omega)\} = \{\xi_L(i\omega)\} + [A(i\omega)]^{-1}\{F_h(i\omega)\} \tag{26}$$

whose IFFT is used for obtaining $\{\xi_{NL}(t)\}$, from which other outputs of interest can be extracted, as discussed after Eq. (9).

4.3: Dynamic loads

The mode-displacement loads distribution method[10] was used in this work to extract the net-loads distribution on the wing

$$\{F_W\} = [\bar{K}_W][\Phi_W^{(e)}]\{\xi_W^{(e)}\} = [\bar{M}_W + \tilde{M}_F^{(W)}][\Phi_W^{(e)}][\Omega_W{}^2]\{\xi_W^{(e)}\} \tag{27}$$

where $\tilde{M}_F^{(W)}$ is the matrix of fictitious masses at the interface coordinates, supplemented with zeros at all other degrees of freedom. The coefficient matrices can be prepared from the wing finite-element mass of stiffness matrices and modal data before the simulation starts. Since the integrated loads at the wing-body interface section should be zero when based on the free wing only, we can deduce from Eq. (27) that

$$\{F_{Wroot}\} = -[\bar{M}_F^{(W)}][\Phi_{IW}^{(e)}][\Omega_W{}^2]\{\xi_W^{(e)}\} \tag{28}$$

5 NUMERICAL EXAMPLE OF VARIABLE WING SWEEP ANGLE

5.1: Sweep angle change from 60 to 0 degrees

Separate finite-element beam-type models were constructed for the wing and body-tail units in the configuration shown in Figure 2 with half-wing length of 1.5 *m*. Normal modes were first calculated for the combined model, with the wing connected to the body at a single grid point in 6 degrees of freedom, and with symmetric boundary conditions applied at the center plane. The lowest natural frequency with Λ=0 is 12.7 *Hz* of wing bending. Fictitious masses (FM) were added at the connection points of the substructure models, and separate normal-modes

analyses were carried out in preparation for modal coupling at various sweep angles between 0 and 60 *deg*.

Previous applications of FMs[8,9] indicated that the modal coupling results are insensitive to the size of the FMs, as long as the they are large enough to cause significant local deformations in the substructure normal modes taken into account, and not large enough to cause numerical ill conditioning. To verify this feature, baseline FM set of 1.0 (*Kg* for translations of *Kg-m*^{2} for rotation) for all the wing interface coordinates and 10.0 for the body ones was established. These values are one order of magnitude smaller than the total masses of the respective substructures. The stiffness and mass matrices of Eq. (18), at Λ=0, were used for calculating the symmetric natural frequencies of the coupled structure using Matlab with various factors between 6 and 6*10^5 multiplying the baseline set. The resulting natural frequency of the coupled first-bending mode is compared in Figure 3 with the one obtained directly for the full ANSYS model, vs. the FM multiplication factor. It can be observed that FM factors of 600 to 60,000 yield similarly accurate results. Hence the FM used in the calculations below were selected as 6000 for the wing and 60000 for the body. All the errors of all the coupled natural frequencies up to 500 Hz were less 0.5% in the entire range of considered sweep angles.

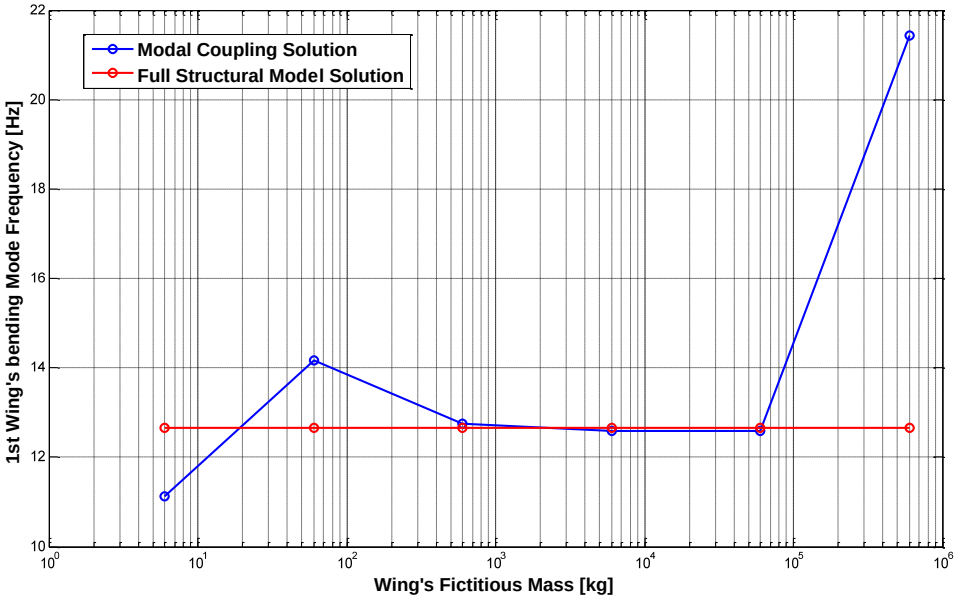

Figure 3 – Fictitious masses size sensitivity

Gust response simulations were performed at *V*=200 *m/sec*, sea level, with a "1-cos" vertical gust with maximal velocity 18 *m/sec*. The 1-cycle gust starts at *t*=0.5 *sec* and last for *T*=0.077 *sec*, which matches the period of the 1st wing frequency. The wing sweep angle changes at a constant rate from Λ=60 *deg* at *t*=0.5 *sec* to 0 *deg* at *t*=1.5 *sec*. The simulations were performed with 16 wing modes and 8 body modes taken into account.

The time history of various aspects of the generalized aerodynamic force on the first bending mode over the entire range of possible sweep values are shown in Figure 4. All the plots are for the same gust excitation and structural response. Each thin line reflects a 1st-wing-bending generalized aerodynamic force in the output vector $\{y_{NL}(t)\}$ of Eq. (25) that would be applied if the sweep angle was fixed at a specific sweep angle. The thick line reflects the actual generalized force that is interpolated from the thin-line response surface according to the

current sweep angle. It starts on the Λ=60 *deg* line at *t*=0.5 *sec* and slides towards the Λ=0 *deg* at *t*=1.5 *sec*, which verifies the force feedback algorithm. It can also be observed that the 1st bending response to the gust dies out in about 1 sec, and that the short-period response lasts much longer, as expected.

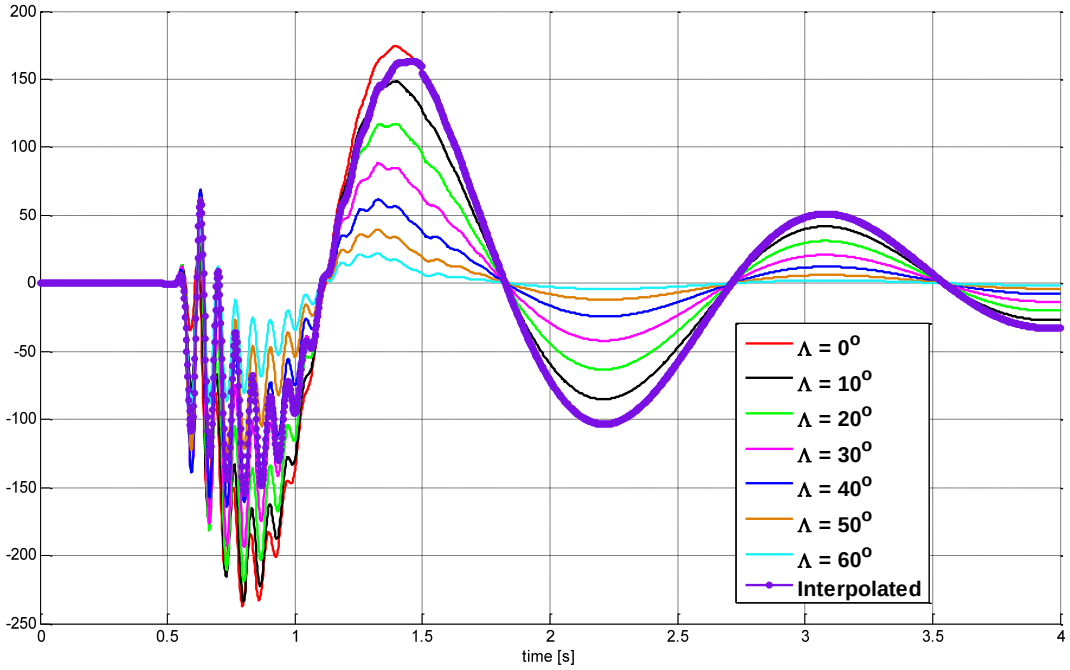

Figure 4: Generalized aerodynamic force on the 1st wing bending mode

Loads parameters right after the gust hits the vehicle in four different $\Lambda(t)$ scenarios are compared in Figure 5. The nominal simulation at which Λ changes from 60 to 0 *deg* is compared to a simulation at the same conditions, but with Λ changing from 0 to 60 *deg*. The cases of fixed sweep angles, with Λ=0 and with Λ=60*deg*, are also shown in Figure 5. The output parameters shown in Figure 5 are the wing-root net shear force, torsion moment, bending moment and the wing-tip vertical acceleration, all in the wing local coordinate system. The section loads were calculated using Eq. (28), and the tip acceleration is the last term of $y_{NL}(t)$ in Eq. (25). It can be observed that the short-period low-frequency response that dominated the aerodynamic response in Figure 4 has a minor effect on the net loads and accelerations in Figure 5. It can also be observed that all the response parameters with a constant Λ=0 have significantly larger peaks than those of Λ=60 *deg*, but they also decay out faster. This is because the lift coefficient is larger at low sweep angles, the aeroelastic effects have a larger effect in reducing the loads at high sweep angels, and also because of the gradual manner in which the gust hits the wing at high sweep angles. The wing-root load peaks with Λ changing from 60 to 0 *deg* are about 10% lower than those with Λ fixed at 60 *deg*, and the peaks with Λ changing from 0 to 60 *deg* are about 10% lower than those with Λ fixed at 0 *deg*.

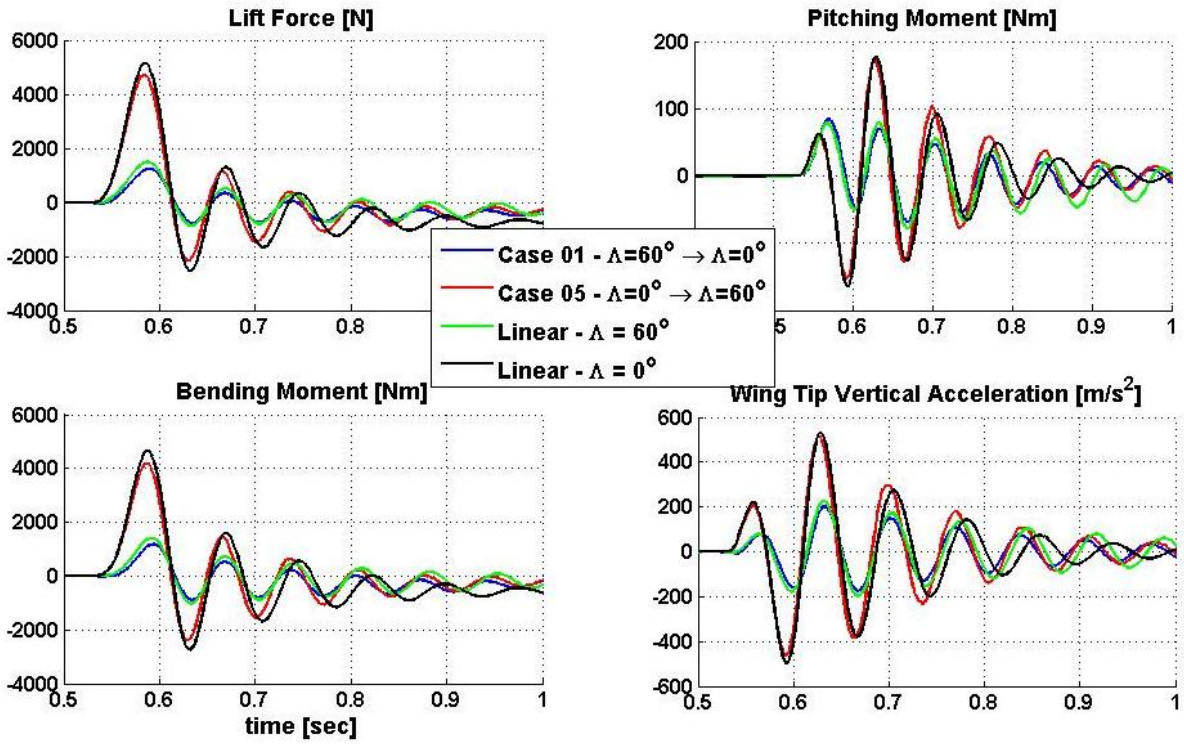

Figure 5: Wing-root section loads and wing-tip vertical acceleration

6 NUMERICAL EXAMPLE OF MANEUVER AND CONTINUOUS-GUST LOADS

Continuous turbulence is described in terms of its Power Spectrum Density (PSD) by the von Kármán expression[13,14] as a function of the frequency. Airworthiness regulations request the calculation of continuous turbulence loads making use of this spectrum with a scale of turbulence of 2500 ft. For a heavy transport aircraft at cruise speed, the von Kármán spectrum is depicted in Figure 6. It can be noted that the energy of the excitation is concentrated at low frequencies, well below the first elastic mode in the following example. This means that rigid-body modes are highly excited and that the low frequency response of the aircraft may be responsible for an important part of the total load.

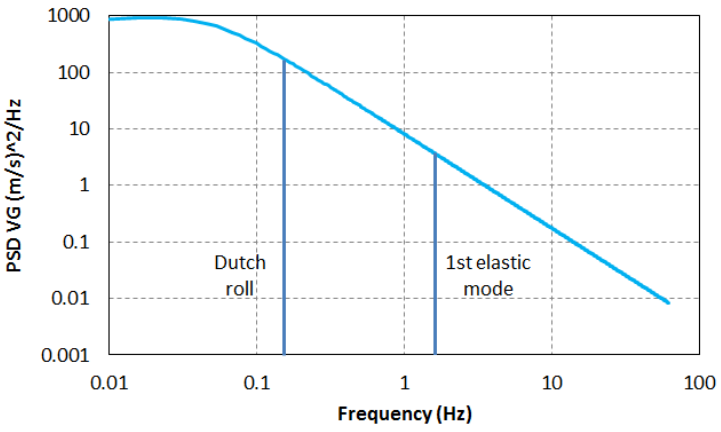

Figure 6: Von Kármán PSD example

Concerning the rigid-body modes[15], standard aeroelastic models can not represent the Phugoid mode, as the flight speed is constant during the analysis. They can not accurately represent the Dutch Roll mode, as the contribution of in-plane motion and forces of the wing are not negligible. On the other hand the Short-Period mode is well represented, specially its frequency, although its damping prediction may be less accurate.

The Dynresp code has been used to supplement the standard continuous turbulence loads calculations with forces modeling the effects not represented by the aeroelastic model. These forces depend on displacements, velocities, angles of attack and aerodynamic loads. The code allows for introducing a high number of sensors and control loops without being unpractical in terms of calculation time.

The aim of this study is to assess the impact of these extra contributions on aircraft dynamic loads. It will be shown that they do not alter gust response loads as they only affect very low frequencies. The work has been focused on the response to lateral turbulence and rudder command. The effects introduced are depicted in Figure 7.

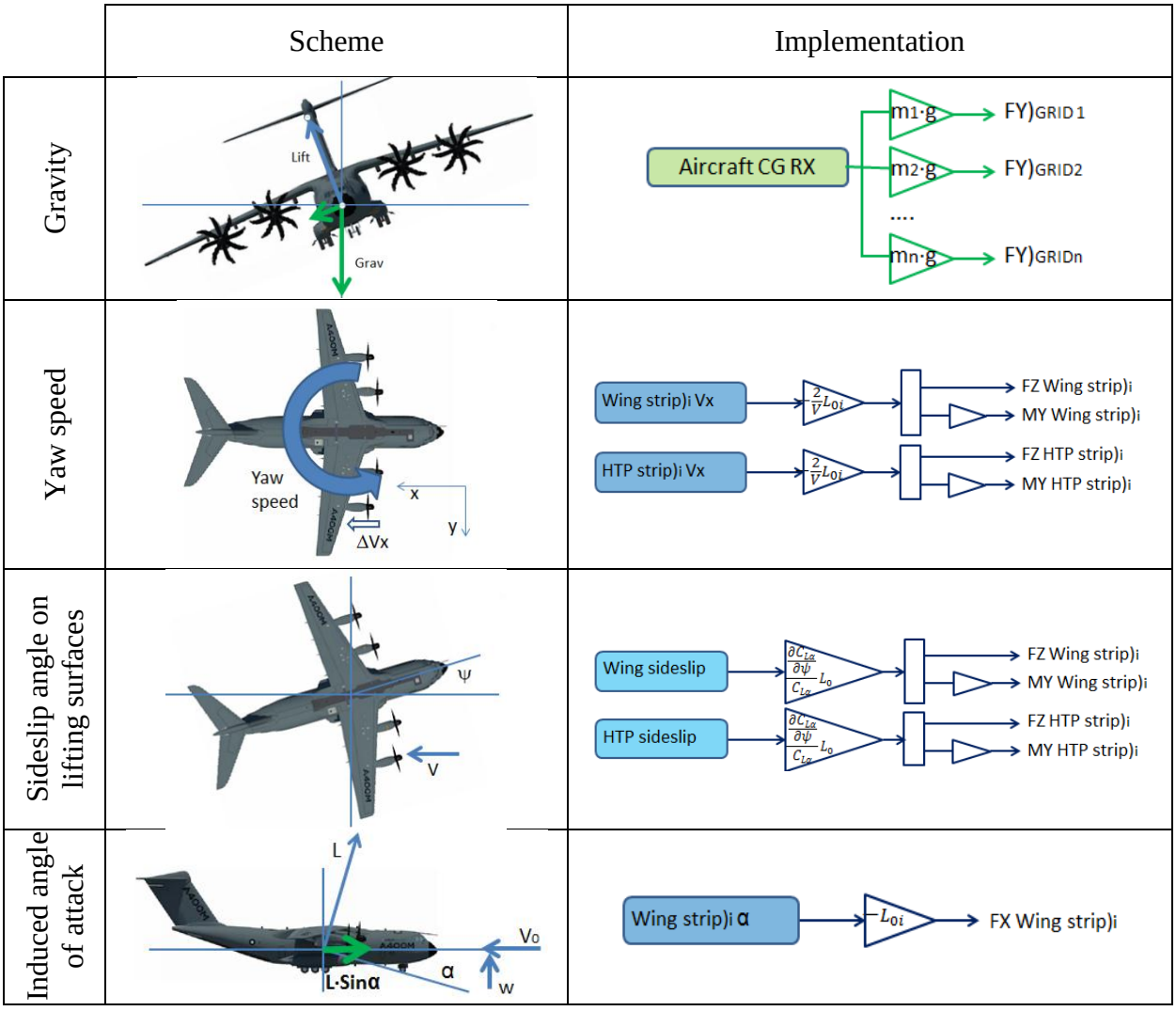

Figure 7: Scheme of the added flight dynamic effects

The following are brief descriptions of the effects in Table 7:

Gravity: This force is taken into account in the steady solution to which dynamic loads are added, but not in the dynamic loads calculation itself. However, when due to a gust or a control command, the aircraft rolls, the lift is no longer vertical with respect to the horizon. In body coordinates, gravity causes lateral acceleration in this case. This has been introduced by applying, at each mass point, a lateral force proportional to the mass value and the roll angle.
Yaw speed: For an aircraft with yaw speed, the wing going into the wind increases its lift due to the increase of apparent speed and proportionally to the wing steady lift. To implement this effect, both the wing and the HTP have been split into strips, and forces have been applied proportional to the steady lift and the increase of speed of each strip.
Sideslip angle on lifting surfaces: When a lifting surface yaws, the apparent sweep angle of each semi-wing changes, changing in turn the local $C_{L\alpha}$[16]. If the angle of attack is constant, this induces a lift variation proportional to the yaw angle and the steady lift. This effect has also been implemented on each wing and HTP strips.
Gust-induced angle of attack: Lift is perpendicular to the wind. During a gust, the local lift direction change is not taken into account in the standard methodology and is introduced here for each wing strip by sensing the local angle of attack.
The impact of other effects have also been studied but resulted in negligible effects. These effects include propellers thrust variation with speed, drag variation due to lift changes in wing and VTP, and tail drag direction changes due to sideslip.

The total number of feedback control loops implemented in Dynresp is 466. The impact of these effects has been assessed by calculating two different responses:

- Response to a rudder sinus-like doublet is shown in Figure 8. The subsequent aircraft trajectory calculated with the aeroelastic model has been compared with the one obtained with a six degrees of freedom non-linear flight simulator used for static and maneuver loads calculation. Rigid aircraft analyses have been used to facilitate the comparison.

- Response to lateral continuous turbulence, expressed by the power spectral density (PSD) of the vertical tail plane (VTP) root bending moment is shown in Figure 9.

Note that the number of feedback control loops may be reduced drastically by taking advantage of Dynresp direct generalized forces for introducing the gravity effect. Instead of one loop per mass, one loop per rigid body mode may be introduced, yielding similar results.

Concerning the aircraft trajectory, the lateral translation (TY) calculated by the simulator (blue) tends to find a new equilibrium position, while the nominal case (red), tends to return to the initial position. The trajectory of the modified model (orange) replicates the simulator behavior. The roll (RX) and yaw (RZ) rotation angle responses reflect the aircraft Dutch Roll motion. The oscillation frequency predicted by the simulator is higher than the one obtained in the nominal case. The effects included in the modified model augment the oscillation frequency and draw the model response closer to the simulator.

The VTP root bending moment PSD of Figure 9 indicates that the main contribution of the added effects to the total load comes from frequencies below 1 Hz, and the peak corresponds to the Dutch-Roll mode. As indicated in Figure 8, the addition of the extra effects increases the Dutch-Roll frequency. Note that the peaks associated with the elastic modes remain unchanged. The inclusion of the extra effects not taken into account in standard lateral continuous turbulence calculations only affects the aircraft low-frequency response, brings

aircraft response closer to the actual trajectory and increases net loads on the VTP root by about 3%.

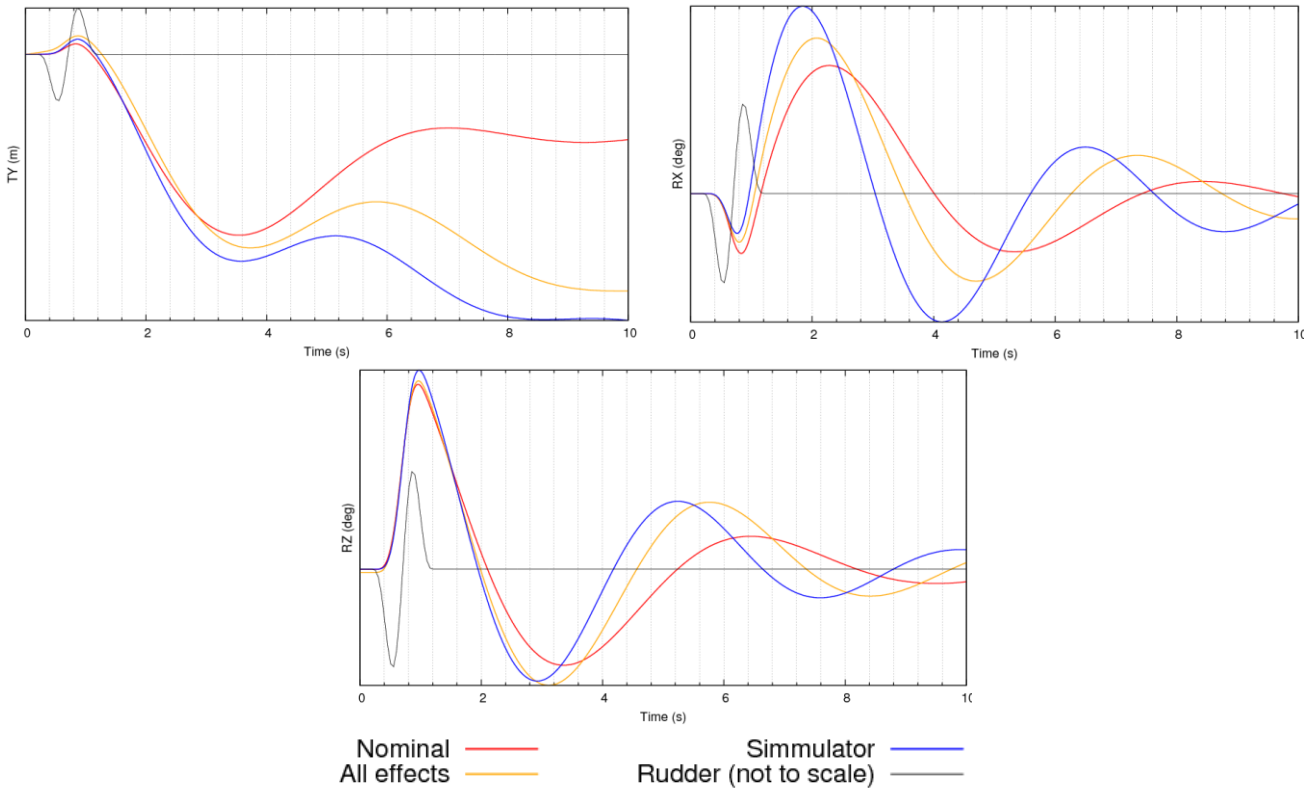

Figure 8: Aircraft trajectory comparison as a response to rudder command

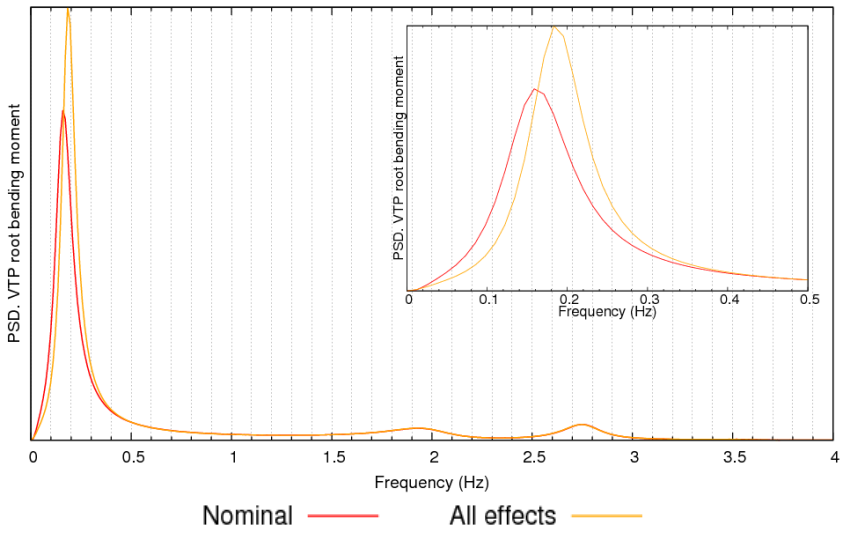

Figure 9: VTP root bending moment PSD as a response to lateral continuous turbulence

7 CONCLUSIONS

New features of the Increased-order-Modeling-based Dynresp framework facilitated the inclusion of direct generalized force inputs and outputs in aeroservoelastic response schemes. The new output option allows the definition of common frequency-domain generalized aerodynamic forces as outputs of the linear model in a way that facilitates their modification by nonlinear feedback loops. It led to the development of a procedure for obtaining dynamic loads to external excitation while the flight vehicle undergoes shape morphing. Parallel generalized aerodynamic force sensors were used to create a dynamic response surface from which actual aerodynamic forces are extracted during the response simulation. The generalized force inputs are then used to for feeding back aerodynamic corrections to yield adequately accurate response histories. The process was applied to a flight vehicle that experiences a discrete-gust excitation while changing it wing sweep angle between 0 and 60 *deg*. The simulation results demonstrated smooth and physically reasonable aerodynamic and net-load response curves during the morphing process, which validates the numerical process. The generalized force feedback was also applied to apply the inertial forces needed in a wing-body modal coupling process that calculates the structural response while the coupling inertia terms are changing with the sweep angle. Fictitious masses added at the interface coordinates of both substructures with errors of less than 0.5% in the lowest 15 natural frequencies over the entire morphing range. Increased-order modeling has also been used to introduce terms usually neglected in continuous turbulence calculations that are important from flight dynamics perspective. The direct generalized force input has been used to reduce the number of feedback control loops. In the example presented, vertical tail net loads are increased by 3% due to the increase of low-frequency response.

8 REFERENCES

1. Karpel, M., “Increased-Order Modeling Framework for Nonlinear Aeroservoelastic Analysis”, Paper No. 2011-73, Proceedings of the International Forum on Aeroelasticity and Structural Dynamics, Paris, France, June 2011.
2. , M. and Shousterman, A., "Combined Frequency and Time-Domain Solutions for Aeroservoelastic Response with Nonlinearities", Proceedings of the International Forum on Aeroelasticity and Structural Dynamics, Bristol, GB, June 2013.
3. Karpel, M., Shousterman, A. Maderuelo, C. Anguita, L., and Climent, H., "Dynamic Gust Response with Nonlinear Control Using Frequency Domain Models", Paper IF-107, Proceedings of the International Forum on Aeroelasticity and Structural Dynamics, Seattle, Washington, June 2009.
4. Karpel, M., Shousterman, A., Maderuelo, C., and Climent, H., “Dynamic Aeroservoelastic Response with Nonlinear Structural Elements”, Proceedings of the 54th AIAA/ASME/ASCE/AHS/ASC Structures, Structural Dynamics, and Materials Conference, Boston, Massachusetts, May 2013.
5. Baldelli, D.H. and Chen, P.C., "Unified Aeroelastic and Flight Dynamic Formulation via Rational Function Approximation", Journal of Aircraft, Vol. 43, No. 3, 2006, pp. 673-772.
6. Selitrennik, E., Karpel, M. and Levy, Y., “Computational Aeroelastic Simulation of Rapidly Morphing Air Vehicles”, Journal of Aircraft, Vol. 49, No. 6, 2012, pp. 1675-1681.
7. Craig, R.R.Jr. and Bampton M.C.C., “Coupling of Substructures for Dynamic Analyses”, AIAA Journal, Vol. 6, No. 7, 1968, pp. 1313-1319.

8. Karpel M., and Raveh D. E., “Fictitious Mass Element in Structural Dynamics”, AIAA Journal, Vol. 34, No. 3, 1996, pp. 607-613.
9. Buchnik S., M. Karpel, “Aeroservoelastic Optimization of Wing with Varying Sweep Angle”, Proceedings of the 55th AIAA/ASMe/ASCE/AHS/SC Structures, Structural Dynamics, and Materials Conference, National Harbor, Maryland, January 2014.
10. Pototzky, A. S., and Perry, B., Ill, "New and Existing Techniques for Dynamic Loads Analyses of Flexible Airplanes," Journal of Aircraft, Vol. 23, No. 4, 1986, pp. 340-347.
11. M. Karpel, E. Presente, “Structural Dynamic Loads in Response to Impulsive Excitation”, Journal of Aircraft, Vol. 32, No. 4, 1995, pp. 853-861.
12. Karpel, M., Shousterman, A., and Mindelis, Y, “Rigid-Body Issues in FFT-Based Dynamic Loads Analysis with Aeroservoelastic Nonlinearities”, Proceedings of the 53rd AIAA/ASME/ASCE/AHS/ASC Structures, Structural Dynamics, and Materials Conference, Honolulu, Hawaii, April 2012.
13. Von Kármán “Progress in the statistical theory of turbulence” Classical papers on Statistical Theory. 1961
14. Houbolt, J.C., Steiner R., Pratt K.G. “Dynamic response of airplanes to atmospheric turbulence including flight data on input and response” NASA TR R-199, June 1964
15. Yechout, Morris, Bossert, Hallgren. “Introduction to Aircraft Flight Mechanics: Performance, Static Stability, Dynamic Stability and Classical Feedback Control”. AIAA Educational Series, 2003
16. Jones, Cohen. “High Speed Wing Theory”. Princeton Aeronautical Paperback, No 6. 1960

9 ACKNOWLEDGEMENT

The work presented in this paper has been partially supported by Grant Agreement CSJU-GAM-SFWA-2008-001 in the framework of the CleanSky-FP7 project.

10 COPYRIGHT STATEMENT